

A Novel Variable-Diameter-Stiffness Cable-Driven Serpentine Manipulator: Design, Modeling, and Characterization

Deshan Meng, *Member, IEEE*, Taowen Guo, Zhihao Ma, Ruiqi Wang, Ziwei Wang, *Member, IEEE*, Xinliang Li, Xueqian Wang*, *Member, IEEE*, and Bin Liang*, *Senior Member, IEEE*

Abstract—Cable-driven serpentine manipulators (CSMs), due to their unique flexibility of movement, have broad application prospects in unstructured and confined environments. To enhance adaptability to different environments and tasks, the design of variable stiffness structures has long been a research focus for CSMs. Inspired by spatial folding mechanisms like umbrellas, we propose a novel variable-diameter-stiffness cable-driven serpentine manipulator (VDS-CSM). The standout feature of this innovation is its ability to achieve integrated control over both the outer diameter and the stiffness of the manipulator. First, we present the structural design of the novel VDS-CSM, whose outer diameter and stiffness can be continuously adjusted. Secondly, we establish the kinematics, statics, and stiffness models for VDS-CSM. Based on this, we conduct an in-depth study of the manipulator’s stiffness characteristics. Simulation data indicate that the change ratio of the manipulator’s end stiffness is approximately proportional to the square of the change ratio in the manipulator’s outer diameter. Finally, we build a VDS-CSM experimental system. Through experiments, the accuracy of the proposed model for VDS-CSM is verified. The experimental results show that the outer diameter and stiffness of the manipulator can vary by 200% and 400%, respectively.

Index Terms—Cable-driven, serpentine manipulator, variable diameter-stiffness, design and modeling, experiments.

I. INTRODUCTION

CABLE-DRIVEN serpentine manipulators (CSMs) possess unique structural features, high motion flexibility, and good safety, making it increasingly vital in diverse fields. These include medical applications such as minimally invasive surgery [1], [2], industrial tasks like narrow space repair and maintenance [3], nuclear equipment maintenance [4], and

This work was supported in part by Guangdong Basic and Applied Basic Research Foundation under Grant 2024A1515030029 and 2022A1515010543, in part by the National Natural Science Foundation of China under Grant 92248304, in part by the National Key R&D Program of China(2022YFB4701400/4701402), in part by the Shenzhen Science and Technology Program (JCYJ20240813151035046). (*Corresponding authors: Xueqian Wang; Bin Liang.*)

Deshan Meng, Taowen Guo, Zhihao Ma and Xinliang Li are with the School of Aeronautics and Astronautics, Shenzhen Campus of Sun Yat-sen University, Shenzhen 518107, China (e-mail: mengdsh3@mail.sysu.edu.cn; guotw3@mail2.sysu.edu.cn; mazhihao@qiyuanlab.com; lixliang8@mail.sysu.edu.cn).

Ruiqi Wang and Bin Liang are with the Department of Automation, Tsinghua University, Beijing 100084, China (e-mail: ruiqi-wa22@mails.tsinghua.edu.cn; liangbin@tsinghua.edu.cn).

Ziwei Wang is with the School of Engineering, Lancaster University, LA1 4YW, United Kingdom. (e-mail: z.wang82@lancaster.ac.uk).

Xueqian Wang is with Shenzhen International Graduate School, Tsinghua University, Shenzhen 518055, China (e-mail: wang.xq@sz.tsinghua.edu.cn).

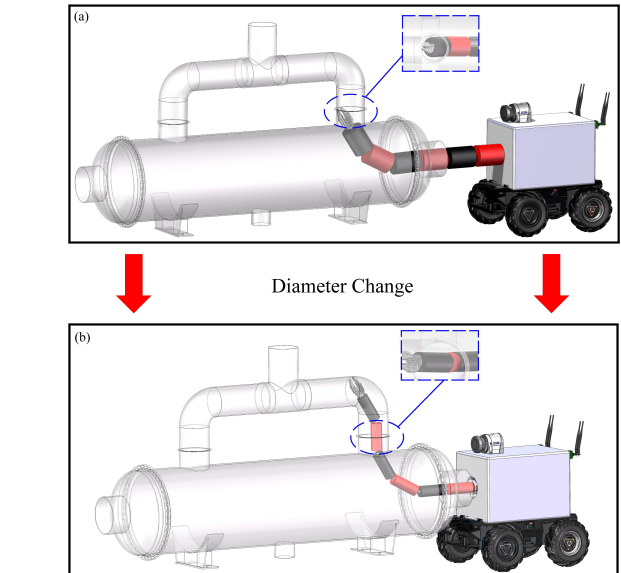


Fig. 1. CSM operation task scene. (a) Before the diameter changes. (b) After the diameter changes.

aerospace applications such as space station monitoring and on-orbit services [5], [6]. Therefore, CSMs have become a research focus in the field of robotics [7]–[9].

A CSM, designed to tackle a broader range of tasks and navigate through complex work environments, must possess the adaptability to alter its stiffness characteristics and structural dimensions. This adaptability is crucial for ensuring that the manipulator can effectively respond to varying conditions, such as different payloads, terrains, and spatial constraints. As shown in Fig.1, when grasping a target within a curved pipe that has an inner diameter smaller than manipulator’s outer diameter, the manipulator must have autonomous diameter-adjustment capability.

A significant amount of research has been conducted on variable stiffness of CSM. Cheng *et al.* [10] proposed using particle jamming technology to adjust the stiffness of manipulator. This method effectively controls local stiffness. Kim *et al.* [11] designed a manipulator with a variable neutral line to adjust stiffness through mechanism changes, which greatly simplifies the mechanical structure. Kang *et al.* [12] proposed the use of shape memory alloy (SMA) to adjust the stiffness

of manipulator, thereby expanding its range of stiffness. Ren *et al.* [13] achieved variable stiffness in manipulator using a spring-sliding block-based drive system, providing high payload, accuracy, and flexibility. Additionally, some scholars have refined stiffness models or optimized control methods to achieve variable stiffness [14]–[16]. The above variable stiffness method exhibits a limited stiffness variation range and poses challenges in achieving accurate control.

In most previous researches, manipulators have maintained a constant geometric profile and structural form [17]–[19]. Lacking the ability to change their external dimensions, manipulators face significant challenges when operating in complex environments or navigating narrow, tortuous paths. In response to this problem, many scholars have studied the transformable manipulator. Liu *et al.* [20] presented a new design for extensible manipulator and demonstrated its extensibility by performing a pin-hole assembly task. Yuan *et al.* [21] proposed a variable cross-section manipulator, which has larger deflections and is softer than constant cross-section manipulator. Burgner-Kahrs *et al.* [22] proposed a tendon-driven continuum robot with extensible sections, greatly increasing the volume of workspace. Wang *et al.* [23] designed a robot with self-controlled curvature to enhance its adaptability in constrained environments. However, the above robots have not achieved integrated adjustment of shape and stiffness.

Regarding the stiffness regulation method of CSM is the focus of attention, but there are fewer research results on how the CSM can realize the autonomous change of structural shape. In the future, CSMs will need to possess the ability to adjust both their structural shape and stiffness to address a variety of tasks and complex working environments. In this article, we propose a novel variable-diameter-stiffness cable-driven serpentine manipulator (VDS-CSM). Enhancements in the mechanism design provide manipulator with strong environmental adaptability and operational capability. The main innovations are as follows.

- 1) A CSM with integrated adjustments for outer diameter and stiffness is designed. This innovative design employs an umbrella skeleton-type variable diameter unit, enabling the stiffness of manipulator to vary exponentially with the outer diameter. The synchronous variable diameter mechanism of driving device prevents coupling between cable and variable diameter unit, ensuring precise manipulator control.
- 2) The kinematic, static, and stiffness models of VDS-CM are meticulously developed, based on which the stiffness characteristics of VDS-CSM have been thoroughly investigated.
- 3) We built an experimental system of VDS-CSM and verified its ability to change diameter and stiffness. Additionally, it has shown significant potential in complex working conditions and industrial production.

The rest of this article is organized as follows. Section II introduces the innovative design of VDS-CSM, which includes the umbrella skeleton type variable diameter unit and the synchronous variable diameter mechanism of driving device. The kinematics, statics, and stiffness models of VDS-

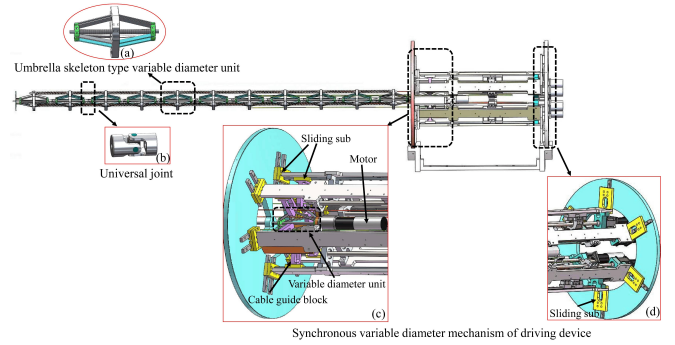


Fig. 2. Schematic diagram of VDS-CSM. (a) Umbrella skeleton type variable diameter unit. (b) Universal joint. (c) Front-synchronous variable diameter mechanism of driving device. (d) Rear-synchronous variable diameter mechanism of driving device.

CSM are derived in Section III. In Section IV, the stiffness characteristics of VDS-CSM is studied. Section V describes the construction of prototype and verifies its integrated adjustment capabilities for outer diameter and stiffness through experiments. Finally, Section VI concludes this article.

II. DESIGN

A. Overview of VDS-CSM

The VDS-CSM proposed in this article is shown in Fig. 2, comprising a diameter-stiffness adjustable arm segment and a driving box. The functions and characteristics of each part are outlined as follows.

1) *Diameter-stiffness variable manipulator*: This part is composed of two main components in series: the umbrella skeleton type variable diameter unit [Fig. 2(a)] and the cross shaft universal joint [Fig. 2(b)]. Each unit is equipped with springs to enhance the stiffness of manipulator.

2) *Driving Control Box*: It is primarily composed of synchronous variable diameter mechanisms at both front [Fig. 2(c)] and rear [Fig. 2(d)], cable guide blocks, motors, and other components. The variable diameter mechanism synchronizes changes in the driving device and the outer diameter of manipulator, thereby preventing coupling between cable and unit due to diameter variations.

The motion of manipulator depends on the coordinated control of motors located at the back end of driving box. These motors pull cables to bend manipulator, enabling its flexible movement. A motor at the front of driving box connects to a threaded mechanism that adjusts the diameter of umbrella skeleton type variable diameter unit through screw transmission. This mechanism allows for integrated adjustment of the manipulator's overall outer diameter and stiffness.

B. Diameter-Stiffness Variable Unit

To enable the VDS-CSM to adjust its outer diameter and stiffness, we conducted in-depth research on the rigid folding mechanism [24], [25]. The umbrella is widely used in space folding mechanisms. When umbrella is opened and closed, the axial size of umbrella bone remains unchanged, while the radial size changes synchronously with the axial movement

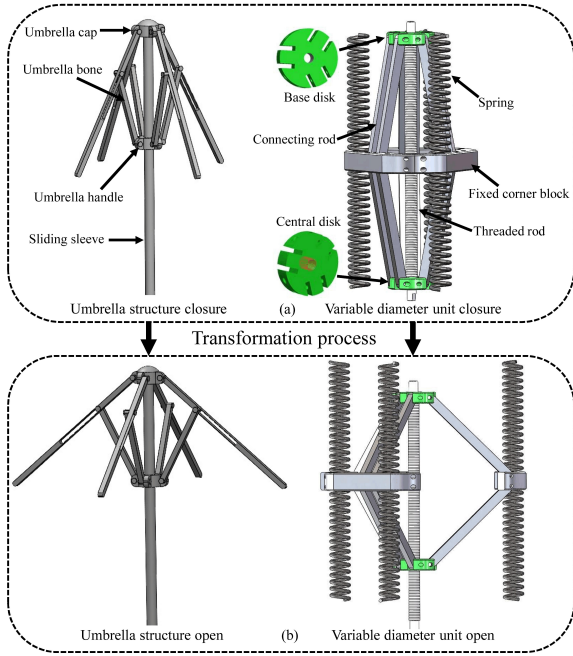


Fig. 3. The transformation process of umbrella skeleton type variable diameter unit. (a) Closed state. (b) Expand state.

of sliding sleeve. Inspired by this space-folding concept, we designed the umbrella skeleton type variable diameter unit for manipulator. The stiffness of VDS-CSM is adjusted by changing the distance between springs and threaded rod axis. Fig. 3 illustrates the schematic diagram of umbrella skeleton type variable diameter unit.

The umbrella skeleton type variable diameter unit consists of a central disk, a base disk, three fixed corner blocks, twelve connecting rods, a threaded rod, and springs. The central disk has a threaded hole, forming a helical pair with threaded rod. The base disk contains a through hole, which forms a sliding pair with the smooth part of threaded rod. In Fig. 2(c), the motor drives threaded rod to rotate forward, causing the central disk to move along the threaded rod towards the base disk via screw transmission. This movement reduces the distance between two disks while increasing the outer diameter of umbrella skeleton type variable diameter unit. To maintain stiffness and curvature after bending, we place springs between variable diameter units and utilize threaded rods and universal joints for joint support.

To further analyze the variation characteristics and capabilities of the variable diameter unit, we established a theoretical model of umbrella skeleton type variable diameter unit, as illustrated in Fig. 4(a). Here, h represents the distance between two disks, l denotes the length of connecting rod, b denotes the radius of two disks, and r represents the outer diameter of manipulator. The outer diameter of VDS-CSM, the length of the connecting rod of variable diameter unit, and the distance between two disks satisfy the following relationship:

$$r = \sqrt{l^2 - \left(\frac{h}{2}\right)^2} + b \quad (1)$$

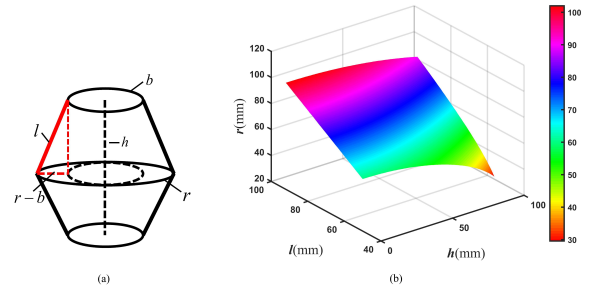


Fig. 4. Characteristic analysis. (a) Theoretical model of variable diameter unit. (b) Variation of the outer diameter. Eq. (1) illustrates the influence of distance h between two disks and length l of connecting rod on the outer diameter.

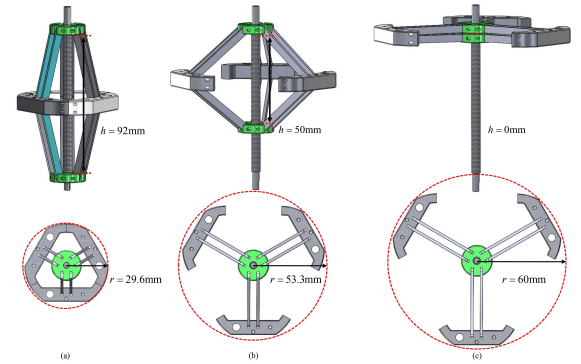


Fig. 5. Conformational and dimensional parameters of the three transformation stages of the umbrella skeleton type variable diameter unit. (a) The first stage. (b) The second stage. (c) The third stage.

From the configuration of variable diameter unit, it is essential to ensure that the outer diameter of manipulator is minimized when three fixed angle blocks are closed. Therefore, the length l of the connecting rod and the distance h between two disks must satisfy specific criteria: $l \geq h/2$. The simulation results illustrating the relationship between outer diameter r of VDS-CSM and variables h and l are shown in Fig. 4(b). As the length l of connecting rod increases, the distance h between the disks decreases, resulting in a larger outer diameter r .

To visualize the relationship between outer diameter r and distance h between two disks, we selected the length of connecting rod $l = 50$ mm, and the radius of disk $b = 10$ mm as variables in three deformation stages of umbrella skeleton type variable diameter unit. We measured the VDS-CSM's outer diameter profile at these stages and compared the results with those obtained from the calculation using (1). The findings are presented in Fig. 5.

C. Driving Control Box

The VDS-CSM contains a large number of cable-hole contact structures. As shown in Fig.6, the acute angle ξ between cable and cable hole axis is too large to cause strong friction. The friction within the cable hole dissipates energy in the manipulator system, leading to attenuation of the cable force during transmission. This affects the length of cable movement and the control accuracy of VDS-CSM. Additionally, when the

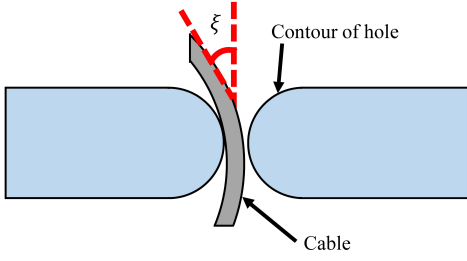


Fig. 6. Schematic diagram of cable through the hole.

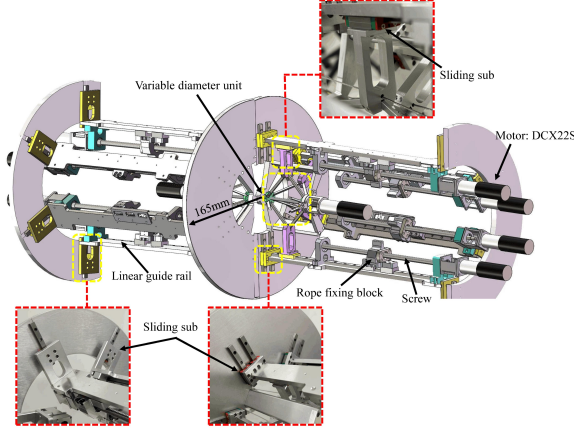


Fig. 7. Sectional view of driving box.

outer diameter of VDS-CSM changes, the distance between driving cables in each group also changes. This increases the angle ξ between cable and cable hole, resulting in a coupling effect.

Based on the mechanism characteristics of VDS-CSM, we designed a synchronous variable diameter mechanism to ensure that drive device changes synchronously with the outer diameter of manipulator, achieving effective decoupling. The mechanism mainly consists of two sets of sliding pairs on the front and rear supports of driving box, and a section of variable diameter unit inside the driving box, as shown in Fig. 7. The front support of driving box is equipped with a guide rail slider along both radial and axial directions. The radial slider is connected to the front part of the ball screw and secured on the guide rail. The rear support of driving box is fitted with a radial guide rail slider, with slider connected to the tail of ball screw. The variable diameter unit inside the driving box is linked to the front guide rail slider through cable guide block. As the outer diameter of manipulator changes, the ball screw moves radially with the slider to achieve synchronous adjustment. The guide rail slider is selected as the mobile device. Compared to ball screws, worm gears, and other mechanisms, it enhances transmission efficiency by approximately 20% and provides greater ease of installation. Simultaneously, the front support of the driving box features a fan-shaped groove for cables to pass through and move, ensuring the smooth operation of the manipulator.

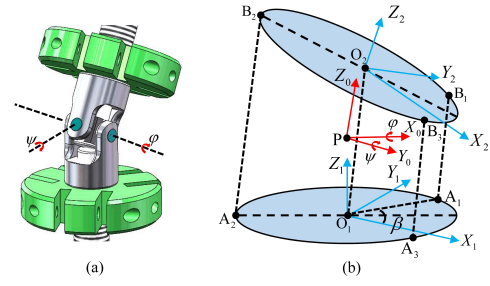


Fig. 8. Kinematic analysis of the joint. (a) Universal joint. (b) Kinematic geometric model.

III. MODELING

A. Kinematics Model

As shown in Fig. 8(b), the point P at the center of joint is identified. The distance from this point to two groups of fixed corner blocks is noted d_A, d_B , and the radius of circumference of cable hole on the fixed corner block is denoted as r_c . In the kinematics model, a change in the outer diameter of VDS-CSM causes a corresponding change in circumference radius (r) of the fixed corner block and the circumference radius (r_c) of the cable hole. The analysis is conducted using one of the joints of VDS-CSM as an example. Take the center of three cable holes A_1, A_2, A_3 on a group of fixed corner block as the origin O_1 , the normal vector of block surface as the Z_1 -axis, and the axis of rotation as the X_1 -axis. Determine the Y_1 -axis according to the right-hand rule, and establish a coordinate system $O_1 - X_1Y_1Z_1$. Take the center of three cable holes B_1, B_2, B_3 on the other group of fixed corner blocks as the origin O_2 , the normal vector of the block surface as the Z_2 -axis, and the axis of rotation as the Y_2 -axis. Determine the X_2 -axis according to the right-hand rule, and establish a coordinate system $O_2 - X_2Y_2Z_2$. The coordinate system $P - X_0Y_0Z_0$ is established with point P as the origin. The X_0 -axis is parallel to the X_1 -axis, the Y_0 -axis is parallel to the Y_1 -axis, and the Z_0 -axis is determined according to the right-hand rule. The coordinate system $O_1 - X_1Y_1Z_1$ is translated d_A along its Z_1 -axis, and then rotated φ angle around the X_1 -axis, which can coincide with the coordinate system $P - X_0Y_0Z_0$. Coordinate system $P - X_0Y_0Z_0$ rotates ψ angle around its Y_0 -axis, and after d_B translations along its Z_0 -axis, it can coincide with coordinate system $O_2 - X_2Y_2Z_2$.

The homogeneous transformation matrix from the coordinate system $O_1 - X_1Y_1Z_1$ to the coordinate system $O_2 - X_2Y_2Z_2$ can be obtained:

$${}^1T_2 = {}^1T_0 {}^0T_2 = \begin{bmatrix} c_\psi & 0 & s_\psi & d_B s_\psi \\ s_\varphi s_\psi & c_\varphi & -s_\varphi c_\psi & -d_B s_\varphi c_\psi \\ -c_\varphi s_\psi & s_\varphi & c_\varphi c_\psi & d_B c_\varphi c_\psi + d_A \\ 0 & 0 & 0 & 1 \end{bmatrix} \quad (2)$$

where $s_\varphi = \sin \varphi, c_\varphi = \cos \varphi, s_\psi = \sin \psi, c_\psi = \cos \psi$.

Assuming $\angle A_1 O_1 X_1 = \angle B_1 O_2 X_2 = \beta$, the point A_1 in coordinate system O_1 is ${}^1A_1 = [r_c \cos \beta \quad r_c \sin \beta \quad 0 \quad 1]^T$, and the point B_1 in coordinate system O_2 is ${}^2B_1 =$

TABLE I
D-H PARAMETERS OF THE SEGMENT

Link $1,i$	a_i (mm)	α_i (degree)	d_i (mm)	$\theta_{1,i}$ (degree)
1	0	90	0	θ_1
2	j	0	0	θ_2
3	0	-90	0	θ_3
4	j	0	0	θ_4
...
11	0	-90	0	θ_{11}
12	j	0	0	θ_{12}

$[r_c \cos \beta \quad r_c \sin \beta \quad 0 \quad 1]^T$. According to (2), the distance between the point A_1 and the point B_1 is:

$$l_{A_1 B_1} = \|\mathbf{B}_1 - \mathbf{A}_1\| = f(\varphi, \psi, \beta) \quad (3)$$

Because the cable holes are evenly distributed on the disk, it can be concluded that:

$$l_{A_2 B_2} = \|\mathbf{B}_2 - \mathbf{A}_2\| = f\left(\varphi, \psi, \beta + \frac{2\pi}{3}\right) \quad (4)$$

$$l_{A_3 B_3} = \|\mathbf{B}_3 - \mathbf{A}_3\| = f\left(\varphi, \psi, \beta - \frac{2\pi}{3}\right) \quad (5)$$

Equations (3), (4), and (5) establish the mapping relationship between joint angle and cable length. Sometimes, it is necessary to determine the joint angle given a specific cable length. Based on above equations, we can obtain the corresponding cable length from the joint angle and then derive the cable speed. The mapping between the rate of change in cable length and the joint angular velocity can be expressed by (6). Here, \mathbf{J}_d is the Jacobian matrix relating the joint angular velocity to the cable velocity. The total length of the cable can be determined using the method described in [6].

$$\begin{bmatrix} \dot{l}_{A_1 B_1} \\ \dot{l}_{A_2 B_2} \\ \dot{l}_{A_3 B_3} \end{bmatrix} = \mathbf{J}_d \begin{bmatrix} \dot{\varphi} \\ \dot{\psi} \end{bmatrix} \quad (6)$$

The mapping from cable length to joint angle can be expressed by (7), where \mathbf{J}_d^+ is the pseudo-inverse matrix of the Jacobian matrix \mathbf{J}_d . According to (7), the corresponding joint rotation angle is calculated using an iterative method.

$$\begin{bmatrix} \dot{\varphi} \\ \dot{\psi} \end{bmatrix} = \mathbf{J}_d^+ \begin{bmatrix} \dot{l}_{A_1 B_1} \\ \dot{l}_{A_2 B_2} \\ \dot{l}_{A_3 B_3} \end{bmatrix} \quad (7)$$

The arm segment of VDS-CSM is composed of multiple orthogonal universal joints and rigid connecting rods in series. The D-H notation is used to construct the coordinate system at each joint of manipulator. Three segments of arm (comprising six joints) in VDS-CSM are considered, with the arm link simplified into a horizontal line. A coordinate system is established at each joint, as shown in Fig. 9. Based on the kinematics model, the D-H parameter table is constructed, as shown in Table I.

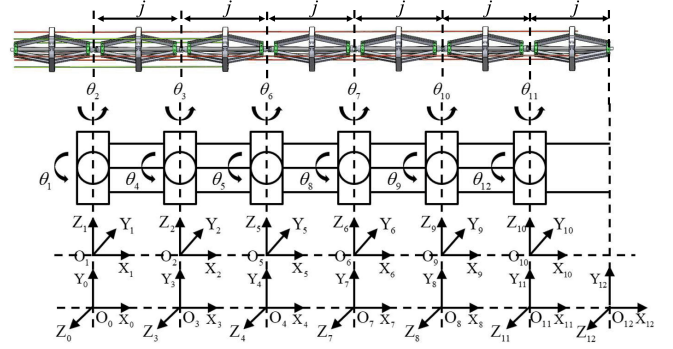


Fig. 9. The coordinate system of segment.

According to D-H parameters, the kinematics of the segment can be expressed as:

$${}^i T_{i+1} = \begin{bmatrix} c_{i+1} & -\lambda_{i+1}s_{i+1} & \mu_{i+1}s_{i+1} & a_{i+1}c_{i+1} \\ s_{i+1} & \lambda_{i+1}c_{i+1} & -\mu_{i+1}c_{i+1} & a_{i+1}s_{i+1} \\ 0 & \mu_{i+1} & \lambda_{i+1} & d_{i+1} \\ 0 & 0 & 0 & 1 \end{bmatrix} \quad (8)$$

where ${}^i T_{i+1}$ is the transformation matrix between two neighboring coordinate systems. Also note $s_{i+1} = \sin \theta_{i+1}$, $c_{i+1} = \cos \theta_{i+1}$, $\mu_{i+1} = \sin \alpha_{i+1}$, $\lambda_{i+1} = \cos \alpha_{i+1}$. Similarly, the forward kinematics of the remaining sections of VDS-CSM, including the end, can be derived using the above method. The end position of VDS-CSM is obtained as follows:

$$\begin{aligned} \mathbf{T}_{\text{end}} &= {}^0 T_1 {}^1 T_2 {}^2 T_3 {}^3 T_4 \cdots {}^{10} T_{11} {}^{11} T_{12} \\ &= \mathbf{f}_{\text{CVDM}}(\theta_1, \theta_2, \theta_3, \theta_4, \dots, \theta_{11}, \theta_{12}) \\ &= \mathbf{f}_{\text{CVDM}}(\boldsymbol{\theta}) \end{aligned} \quad (9)$$

where $\mathbf{f}_{\text{CVDM}}(\boldsymbol{\theta})$ is the simplified kinematics equation of VDS-CSM, and $\boldsymbol{\theta}$ is the column vector composed of $\theta_1 \sim \theta_{12}$.

For the m -segment (a single segment of VDS-CSM contains two variable diameter units), the position of the end of VDS-CSM can be expressed as follows:

$$\mathbf{T}_m = \mathbf{f}_{\text{CVDM}}(\theta_1, \theta_2, \theta_3, \theta_4, \dots, \theta_{2m}) \quad (10)$$

Inverse kinematics analysis is useful for studying the trajectory planning of VDS-CSM, as well as improving the control accuracy and response time of manipulator. For the CSM, the iterative method proposed by Whitney [26] is often used to solve the inverse kinematics. By solving the Jacobian matrix for each joint variable, it can be shown that there is a minimum norm solution in the velocity domain. The desired position of the end of VDS-CSM in space is calculated, and the position difference is obtained by subtracting it from the current position. Through the Jacobian matrix, the position difference of VDS-CSM is mapped to the joint angles.

$$\dot{\mathbf{X}} = \mathbf{J}_\theta(\boldsymbol{\theta})\dot{\boldsymbol{\theta}} \quad (11)$$

where \mathbf{J}_θ is the Jacobian matrix of the joint velocity to the end velocity, and from (11), the relationship between the differential of the joint angle and the differential of the end position is given by:

$$\Delta \boldsymbol{\theta} = \mathbf{J}_\theta^+ \Delta \mathbf{X}_{\text{end}} \quad (12)$$

In (12), \mathbf{J}_θ^+ is the pseudo-inverse matrix of \mathbf{J}_θ . Iteratively calculate the position variation to obtain the angle of each joint, enabling the VDS-CSM to complete the target motion. By comparing the difference between the current position and the expected position, when the difference is less than the threshold value, it is considered that VDS-CSM has reached the target position.

B. Statics Model

Due to the low velocity during the movement of VDS-CSM, it is considered to be in a state of static equilibrium. According to (6), the transfer relationship between cable tension and joint torque can be derived from the principles of duality and virtual work:

$$\boldsymbol{\tau} = \mathbf{J}_d^T \mathbf{f} \quad (13)$$

where $\boldsymbol{\tau} = [\tau_\varphi, \tau_\psi]^T$, $\mathbf{f} = [f_1, f_2, f_3]^T$ indicates the joint torque and the tension of three cables, and \mathbf{J}_d^T is the transpose of the velocity Jacobian matrix \mathbf{J}_d . Similarly, the transfer relationship between joint torque of VDS-CSM and the end operating force can also be obtained by the above method:

$$\boldsymbol{\tau} = \mathbf{J}_\theta^T \mathbf{F}_e \quad (14)$$

where \mathbf{J}_θ^T indicates the force Jacobian matrix, which is the transpose of the velocity Jacobian matrix \mathbf{J}_θ , \mathbf{F}_e represents the generalized end force vector.

The VDS-CSM experiences various forces during its operation, including its own gravity, end loads, driving cable tension, spring elasticity, and friction between cable and cable hole. Considering that lubrication measures can reduce friction between cable and cable hole, the friction coefficient is neglected in the static model. By applying the principle of virtual work, we obtain:

$$\mathbf{F}_e^T \delta \mathbf{X} - \mathbf{T}_c^T \delta \mathbf{L}_c - \mathbf{T}_s^T \delta \mathbf{L}_s - \mathbf{G}^T \delta \mathbf{H} = 0 \quad (15)$$

$$\mathbf{T}_s = \mathbf{T}_a + \mathbf{T}_b \quad (16)$$

where \mathbf{X} is the generalized coordinate, \mathbf{T}_c is the generalized tension vector consisting of all cable tensions, and \mathbf{T}_s is the generalized elastic force vector consisting of all spring elastic forces. The spring elastic forces \mathbf{T}_s includes the axial elastic force \mathbf{T}_a when the spring is stretched or compressed, and bending elastic force \mathbf{T}_b when it is bent. \mathbf{L}_c is the generalized cable length vector, \mathbf{L}_s is the generalized spring length vector, \mathbf{G} is the generalized gravity vector, and \mathbf{H} is the generalized vector composed of the center of gravity position of each section of VDS-CSM.

$\delta \mathbf{X} = \frac{\partial \mathbf{X}}{\partial \boldsymbol{\theta}} \delta \boldsymbol{\theta}$, $\delta \mathbf{L}_c = \frac{\partial \mathbf{L}_c}{\partial \boldsymbol{\theta}} \delta \boldsymbol{\theta}$, $\delta \mathbf{L}_s = \frac{\partial \mathbf{L}_s}{\partial \boldsymbol{\theta}} \delta \boldsymbol{\theta}$, $\delta \mathbf{H} = \frac{\partial \mathbf{H}}{\partial \boldsymbol{\theta}} \delta \boldsymbol{\theta}$ are all substituted into (15) to yield (17)

$$\mathbf{F}_e^T \frac{\partial \mathbf{X}}{\partial \boldsymbol{\theta}} \delta \boldsymbol{\theta} - \mathbf{T}_c^T \frac{\partial \mathbf{L}_c}{\partial \boldsymbol{\theta}} \delta \boldsymbol{\theta} - \mathbf{T}_s^T \frac{\partial \mathbf{L}_s}{\partial \boldsymbol{\theta}} \delta \boldsymbol{\theta} - \mathbf{G}^T \frac{\partial \mathbf{H}}{\partial \boldsymbol{\theta}} \delta \boldsymbol{\theta} = 0 \quad (17)$$

$\delta \boldsymbol{\theta}$ on both sides of the equation is simultaneously simplified, and the Jacobian matrixes ($\mathbf{J}_X = \partial \mathbf{X} / \partial \boldsymbol{\theta}$, $\mathbf{J}_{L_c} = \partial \mathbf{L}_c / \partial \boldsymbol{\theta}$, $\mathbf{J}_{L_s} = \partial \mathbf{L}_s / \partial \boldsymbol{\theta}$, $\mathbf{J}_H = \partial \mathbf{H} / \partial \boldsymbol{\theta}$) are introduced into (17). We obtain:

$$\mathbf{F}_e^T \mathbf{J}_X - \mathbf{T}_c^T \mathbf{J}_{L_c} - \mathbf{T}_s^T \mathbf{J}_{L_s} - \mathbf{G}^T \mathbf{J}_H = 0 \quad (18)$$

where \mathbf{J}_X , \mathbf{J}_{L_c} , \mathbf{J}_{L_s} , \mathbf{J}_H are the Jacobian matrixes of end effector, cables, springs, and gravity, respectively.

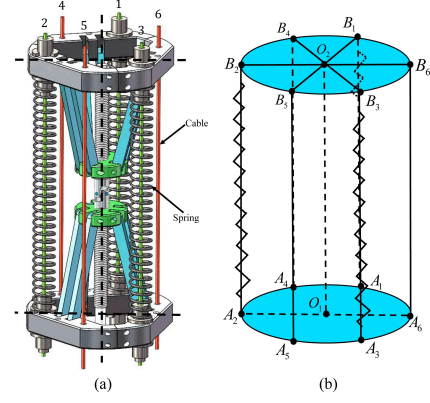


Fig. 10. Stiffness model. (a) Single segment of VDS-CSM. (b) Simplified theoretical models.

C. Stiffness Model

The VDS-CSM adjusts its stiffness by changing the distance between driving cable and spring relative to the central axis of manipulator. This adjustment is achieved by varying the outer diameter of arm segment. The stiffness of VDS-CSM is primarily provided by spring and driving cable. To model the stiffness of manipulator, we assume that the spring conforms to the constant curvature model during bending and that the manipulator does not twist during operation. The single-segment model of VDS-CSM is shown in Fig. 10(b). Springs are placed outside the driving cables at holes 1, 2, and 3, while only driving cables are present at holes 4, 5, and 6, with no spring connections.

As Simaan stated in [27] and [28], after transposing (18), the joint angle $\boldsymbol{\theta}$ is fully differentiated and the Hessian matrix is retained to obtain the following results (the gravity of VDS-CSM is constant, $\mathbf{J}_H^T \frac{\partial \mathbf{G}}{\partial \boldsymbol{\theta}} = 0$):

$$\mathbf{K}_r = \left(\mathbf{J}_X^T \right)^{-1} \left(\begin{array}{l} \mathbf{H}_{J_{L_c}^T} \mathbf{T}_c + \mathbf{J}_{L_c}^T \mathbf{K}_c \mathbf{J}_{L_c} \\ + \mathbf{H}_{J_{L_s}^T} \mathbf{T}_s + \mathbf{J}_{L_s}^T \mathbf{K}_s \mathbf{J}_{L_s} \\ + \mathbf{H}_{J_H^T} \mathbf{G} - \mathbf{H}_{J_X^T} \mathbf{F}_e \end{array} \right) \left(\mathbf{J}_X \right)^{-1} \quad (19)$$

where $\mathbf{K}_r \in \mathbf{R}^{6 \times 6}$ is the stiffness matrix of the end of VDS-CSM in Cartesian space, $\mathbf{K}_c \in \mathbf{R}^{3m \times 3m}$, $\mathbf{K}_s \in \mathbf{R}^{3 \times 3}$ represent the diagonal matrix of the cables and springs stiffness. The end stiffness of manipulator is composed of two parts. The first part, referred to as the end active stiffness, is related to the tension of the cable and the spring. The second part, known as the end passive stiffness, is related to the tensile stiffness of the cable and spring. In fact, the elements in the Hessian matrix $\mathbf{H}_{J_X^T}$, $\mathbf{H}_{J_{L_c}^T}$, $\mathbf{H}_{J_{L_s}^T}$, and $\mathbf{H}_{J_H^T}$ are very small. Therefore, the Hessian matrix is not the main factor influencing the stiffness matrix in (19). To simplify the calculation, the stiffness model, after ignoring the Hessian matrix, can be written as:

$$\mathbf{K}_r = \left(\mathbf{J}_X^T \right)^{-1} \left(\mathbf{J}_{L_c}^T \mathbf{K}_c \mathbf{J}_{L_c} + \mathbf{J}_{L_s}^T \mathbf{K}_s \mathbf{J}_{L_s} \right) \left(\mathbf{J}_X \right)^{-1} \quad (20)$$

From (20), the main factors determining the stiffness of VDS-CSM are \mathbf{J}_X , \mathbf{J}_{L_c} , \mathbf{J}_{L_s} (related to joint angle and outer diameter) and \mathbf{K}_c , \mathbf{K}_s (related to cable and spring stiffness). The joint angle and outer diameter are structural parameters

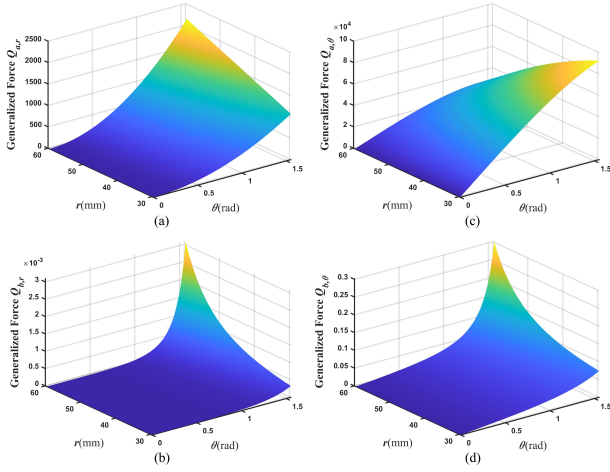


Fig. 11. (a) and (b) show the influence of radius on the axial generalized force Q_a and the bending generalized force Q_b . (c) and (d) illustrate the influence of joint angle on the axial generalized force Q_a and the bending generalized force Q_b . (take $K_a = K_b$)

of VDS-CSM, and their values and variation characteristics are easily determined. Therefore, we primarily discuss the influence of cable and spring stiffness on the stiffness of VDS-CSM. Typically, the stiffness of cable significantly exceeds that of spring. As indicated in (20), the stiffness of cable is highly sensitive to variations in diameter. The stiffness of cable is usually directly determined by its structural parameters, whereas the stiffness of the spring is more complex.

As seen in $K_s = \partial T_s / \partial \theta$, $T_s = T_a + T_b$, the spring's elastic force comprises the axial elastic force generated during stretching or compression, and the bending elastic force produced during bending. These forces give the spring both axial stiffness K_a and bending stiffness K_b . Due to the bending characteristics of spring, the axial stiffness and the bending stiffness are coupled, making it difficult to determine the stiffness of VDS-CSM. To address this issue, we propose a stiffness simplification method for VDS-CSM.

To analyze the influence of the axial and bending elastic forces of spring on the movement of VDS-CSM, we investigate the energy of spring in tension/compression E_a and bending E_b . Assuming that the spring conforms to the constant curvature model in bending, the energy change of the spring is only related to its stiffness K_a , K_b , the joint angle θ , and the radius r of VDS-CSM. The energy of spring is obtained by taking the partial derivatives with respect to the joint angle θ and radius r of VDS-CSM, and the relationship between the axial generalized force Q_a and the bending generalized force Q_b of spring, as well as the joint angle θ and radius r , is determined:

$$\begin{cases} Q_{a,r} = \frac{\partial E_a}{\partial r} \\ Q_{b,r} = \frac{\partial E_b}{\partial r} \end{cases}, \begin{cases} Q_{a,\theta} = \frac{\partial E_a}{\partial \theta} \\ Q_{b,\theta} = \frac{\partial E_b}{\partial \theta} \end{cases} \quad (21)$$

From the longitudinal axis data presented in Fig. 11, it is evident that when θ and r change, the axial generalized force Q_a differs from the bending generalized force Q_b by five orders of magnitude (10^5). Therefore, the bending elastic force Q_b during bending can be ignored. In (21), the diagonal

matrix of cable and spring stiffness can be simplified as (the number of segments, m , is 2):

$$\begin{cases} K_c = \text{diag} \left[\frac{EA}{l_s} & \frac{EA}{l_s} & \frac{EA}{l_s} & \frac{EA}{l_s} & \frac{EA}{l_s} & \frac{EA}{l_s} \right] \\ K_s = K_a = \text{diag} \left[k_a & k_a & k_a & 0 & 0 & 0 \right] \end{cases} \quad (22)$$

where E and A represent the elastic modulus and the cross-sectional area of the cable, respectively, l_s is the initial length of the cable, and k_a is the axial stiffness coefficient of a single spring.

IV. STIFFNESS CHARACTERISTICS ANALYSIS

According to (20), the stiffness at the end of VDS-CSM depends on the joint angle, manipulator's radius, cable stiffness, and spring stiffness. Cable and spring stiffness are inherent material properties that remain constant throughout the manipulator's operation. To further analyze the stiffness variations of VDS-CSM, we examine the joint angle and manipulator's radius as variables affecting the end stiffness. Given the assumption that the VDS-CSM is free of torsion, torsional stiffness at the end is not considered, and the number of segments, m , is 3.

A. The Impact of Arm Radius on End Stiffness

We define the X -axis along the axial direction of the manipulator, the Z -axis along the radial direction, and the Y -axis according to the right-hand rule. Due to the manipulator being in a singular configuration when joint angle $\theta = 0$, an approximate value is chosen for verification instead.

Firstly, in the configuration where the joint angle $\theta \approx 0$ [Fig. 12(a)], the radius of VDS-CSM is continuously adjusted from 29.6 mm to 60 mm, and the change in end stiffness is depicted in Fig. 12(b). Since the manipulator is in a singular configuration, the stiffness along the X -axis approaches infinity. The rate of stiffness increase along the Y -axis and Z -axis is approximately 400%.

Then, under the configuration where the joint angle $\theta = \pi/18$ [Fig. 13(a)], the radius of VDS-CSM is continuously adjusted from 29.6 mm to 60 mm, and the change in end stiffness is shown in Fig. 13(b). The analysis shows that the stiffness increase rate at the end of VDS-CSM reaches approximately 400% in all directions.

According to the analysis above, adjusting the manipulator's radius can effectively increase the end stiffness.

B. The Impact of Joint Angle on End Stiffness

To verify the influence of joint angle on the end stiffness of VDS-CSM, the joint angle is incrementally increased from $\theta = \pi/36$ to $\theta = \pi/12$ under conditions where the radius is set to $r = 30$ mm and $r = 45$ mm, respectively. The simulation results for the end stiffness are depicted in Fig. 14 and Fig. 15.

Based on the above analysis, the stiffness characteristics of VDS-CSM are primarily influenced by the radius and joint angle, which continuously vary with actual working conditions. The manipulator exhibits the following characteristics.

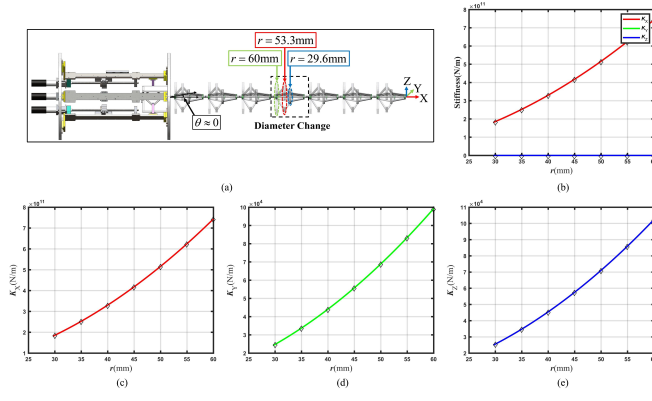


Fig. 12. Radius-stiffness variation characteristics (a) Radius variation of VDS-CSM in joint angle $\theta \approx 0$ configuration. (b) Variation of stiffness at the end of VDS-CSM. (c) The X -axis stiffness. (d) The Y -axis stiffness. (e) The Z -axis stiffness.

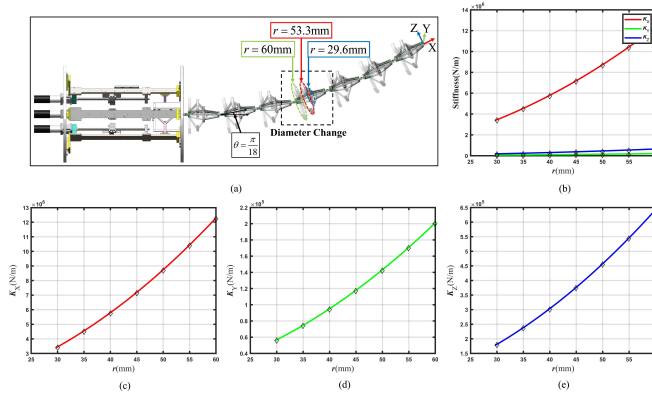


Fig. 13. Radius-stiffness variation characteristics (a) Radius variation of VDS-CSM in joint angle $\theta = \pi/18$ configuration. (b) Variation of stiffness at the end of VDS-CSM. (c) The X -axis stiffness. (d) The Y -axis stiffness. (e) The Z -axis stiffness.

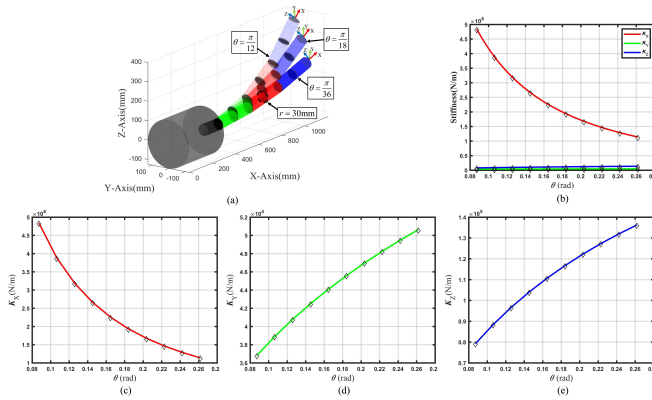


Fig. 14. Joint angle-stiffness variation characteristics (a) Under the configuration where radius $r = 30$ mm, joint angle of VDS-CSM changes. (b) Variation of stiffness at the end of VDS-CSM. (c) The X -axis stiffness. (d) The Y -axis stiffness. (e) The Z -axis stiffness.

- 1) The change ratio of VDS-CSM's end stiffness is approximately proportional to the square of the change ratio in VDS-CSM's outer diameter.
- 2) The change in joint angle is positively correlated with the change in end stiffness and negatively correlated with

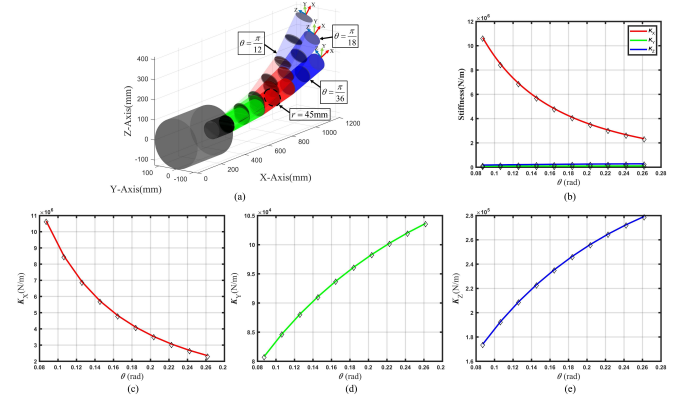


Fig. 15. Joint angle-stiffness variation characteristics (a) Under the configuration where radius $r = 45$ mm, joint angle of VDS-CSM changes. (b) Variation of stiffness at the end of VDS-CSM. (c) The X -axis stiffness. (d) The Y -axis stiffness. (e) The Z -axis stiffness.

the tensile properties of VDS-CSM.

The VDS-CSM's excellent ability to integrate adjustments between outer diameter and stiffness equips it with versatile functionality, making it adaptable to a wide range of task requirements.

V. PROTOTYPE AND EXPERIMENTS

A. Prototype and Experiment Setup

To verify the novel mechanical design, a CSM prototype with an adjustable arm diameter and synchronous stiffness adjustment was developed, as shown in Fig. 16. The prototype arm is divided into two segments, each containing two umbrella skeleton type variable diameter units. The overall structure is constructed from aluminum alloy. The specific dimensions of prototype are as follows: the total length of the arm is 650 mm, and the length of driving box is 415 mm. The driving strategy for the arm involves using a motor to drive and control the cable. Three cables, spaced 120 degrees apart, are used as a group to control each section of joint movement. The motor model is Maxon DCX22S (rated torque: 15.3 mNm, rated speed: 10800 r/min, rated power: 24 W, mass: 66.8 g), the motor planetary gear reducer model is GPX22 A (reduction ratio: 62, mass: 67 g). All motors and reducers are installed inside driving box and controlled by the RoboModule driver. We use a ThinkPad (Core i7, Intel Xe Graphics) as the upper computer and the communication protocol is CAN.

B. Variable Stiffness Model Validation

To verify the diameter-stiffness integrated adjustment capability of VDS-CSM, as shown in Fig. 17, we conducted a load test on manipulator. First, with the manipulator radius set to 32 mm, a 200 g weight was suspended at the end, and the driving force of cable was adjusted to maintain the manipulator in a horizontal position. Next, the manipulator radius was adjusted to 46 mm while keeping it horizontal, allowing it to support a 500 g weight at the end. Finally, the radius was adjusted to the critical state of 58 mm, and the end was able to support a 1000 g weight. As the VDS-CSM's load increases, the end of

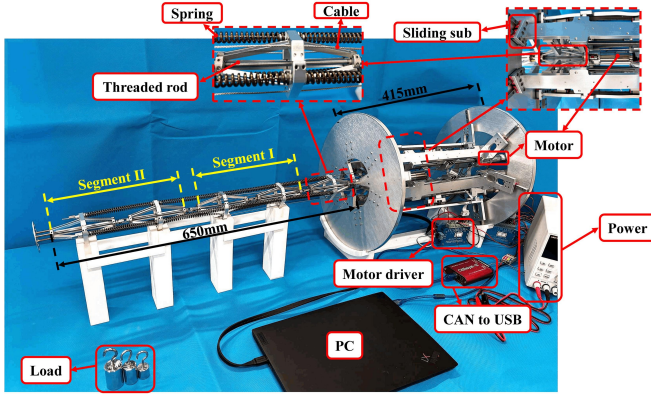


Fig. 16. Prototype and experimental system of VDS-CSM.

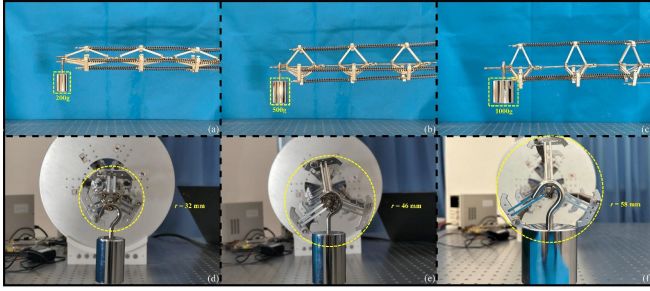


Fig. 17. Diameter-stiffness integrated adjustment test. (a) Load 200 g. (b) Load 500 g. (c) Load 1000 g. (d) Radius is 32 mm. (e) Radius is 46 mm. (f) Radius is 58 mm.

manipulator moves upward by 5 mm, and motor's peak current rises from 109 mA to 175 mA.

When the VDS-CSM is placed horizontally, the theoretical end stiffness calculated using (20) is compared with the end stiffness of VDS-CSM, directly measured using (23). To minimize the influence of external forces and gravity on the experimental results, a 200 g weight was suspended vertically at the end of VDS-CSM to simulate the external force, as shown in Fig. 18(c). During the experimental validation of the theoretical stiffness model and the direct measurement method, the stiffness in the Z -axis direction was used for calculation and comparison. Where K_p is the measured stiffness. ΔF is the external force applied on the end of VDS-CSM. Δz represents the displacement change at the end of VDS-CSM.

$$K_p = \frac{\Delta F}{\Delta z} \quad (23)$$

In the experiment, the NOKOV optical motion capture system was used to measure the displacement change at the end of VDS-CSM after external force was applied at different radius states. Based on the measurement data, the theoretical stiffness, measured stiffness, and error at the end of VDS-CSM are presented in Fig. 19. These experiments validate the accuracy of the stiffness model for VDS-CSM and demonstrate its effective outer diameter-stiffness integration adjustment capability.

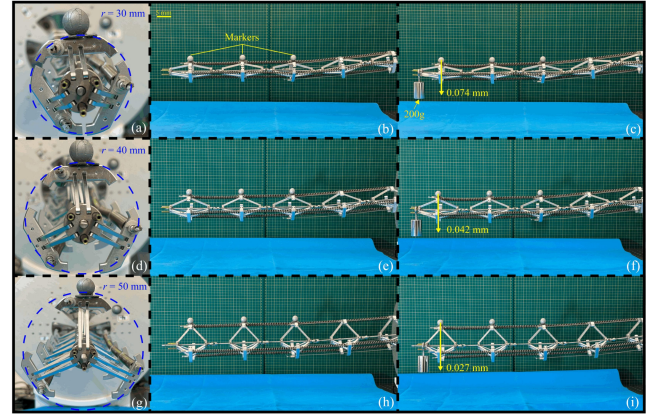


Fig. 18. Experimental validation of theoretical stiffness and measured stiffness comparison. (a) Radius is 30 mm. (b) No-load state. (c) 200 g-load state. (d) Radius is 40 mm. (e) No-load state. (f) 200 g-load state. (g) Radius is 50 mm. (h) No-load state. (i) 200 g-load state.

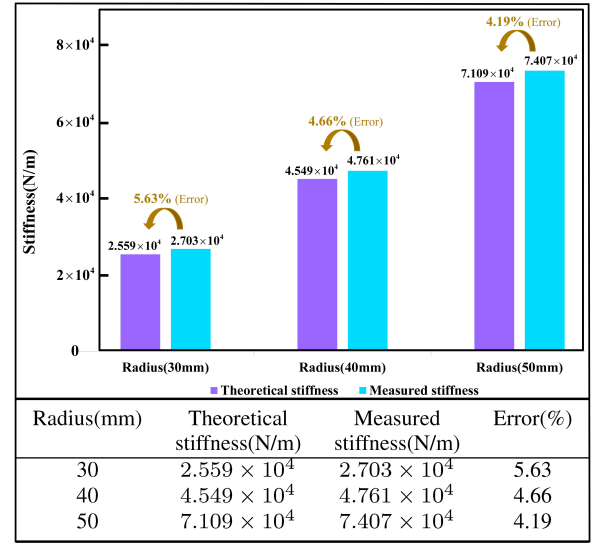


Fig. 19. Theoretical stiffness, measured stiffness, and error.

C. Demonstration of Prototype Functions

To verify the manipulator's performance in complex working conditions, we set up two circles with different radii, as shown in Fig. 20. When VDS-CSM encounters the first circle (70 mm), it adjusts its radius to 55 mm to pass through. For the second circle (40 mm), the radius is adjusted to 35 mm to complete the crossing. For instance, in the maintenance of aerospace equipment characterized by complex structural dimensions, the manipulator can achieve precise operations on the target by dynamically adjusting its outer diameter.

In the handling of medical supplies, VDS-CSM can grasp and move the target using its structural characteristics without relying on an end effector. As illustrated in Fig. 21, we use a cup with an inner diameter of 32 mm and a height of 100 mm as the target, moving it from the white circle to the black circle by utilizing the VDS-CSM's transformation capabilities. First, the VDS-CSM approaches the target, and its end is bent into the cup. The VDS-CSM's outer diameter is then adjusted to match the cup's inner diameter. As the manipulator's stiffness

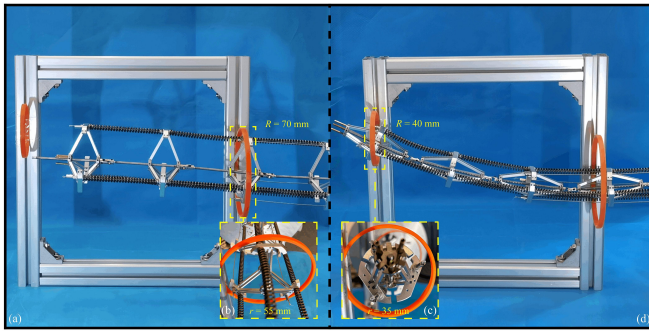


Fig. 20. Variable diameter crossing circulars experiment. (a) When VDS-CSM's radius is 55 mm, it successfully passes through a circle with a radius of 70 mm. (b) Through the first circle. (c) Through the second circle. (d) When VDS-CSM's radius is 35 mm, it successfully passes through a circle with a radius of 40 mm.

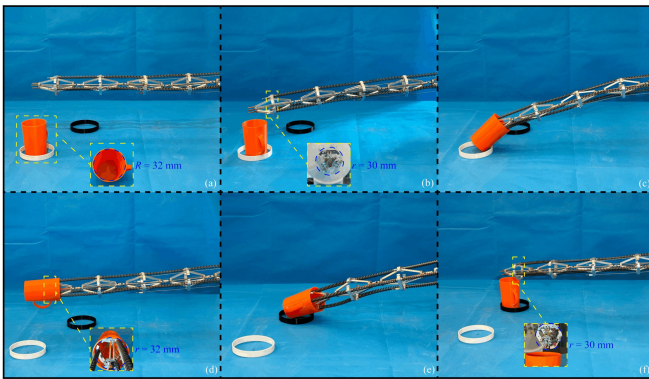


Fig. 21. Target grabbing experiment. (a) Initial state of VDS-CSM. (b) VDS-CSM approaches the target. (c) The end of VDS-CSM bends and extends into the target. (d) The outer diameter of VDS-CSM increases to complete the grab. (e) Adjust the pose of VDS-CSM to move the target. (f) The outer diameter of VDS-CSM decreases.

increases, it grasps the target through friction between the arm segment and the inner wall of the cup, adjusting its position so that the target is placed at the black circle. Finally, the VDS-CSM's outer diameter is reduced to be smaller than the cup's inner diameter, completing the grasping and movement of the target.

VI. CONCLUSION

In order to enhance the navigation and operation capability of CSM in the narrow space with variable constraint dimensions, this article proposes a novel VDS-CSM, which achieves the continuous adjustment of the outer diameter of the manipulator and exponential change of the stiffness by borrowing the umbrella folding mechanism. The detailed kinematics, statics, and stiffness models of VDS-CSM are established, and the relationship between outer diameter and stiffness is analyzed. Furthermore, experiments are designed to verify the variable stiffness model and demonstrate the prototype's functionality. The experimental data demonstrate that the stiffness adjustment range of manipulator is approximately 400%. The VDS-CSM proposed in this article can handle a wider range of tasks and navigate through complex working environments. Changes in diameter alter the inertia

and dynamic characteristics of VDS-CSM, thereby modifying its control parameters and introducing challenges for achieving precise control. In the future, we will continue to study the control issues of VDS-CSM and application exploration for specific mission requirements.

REFERENCES

- [1] Z. Hu, J. Li, and S. Wang, "Design and Kinematics of a Robotic Instrument for Natural Orifice Transluminal Endoscopic Surgery," *IEEE/ASME Trans. Mechatron.*, vol. 28, no. 5, pp. 2840–2851, Oct. 2023.
- [2] M. Rox *et al.*, "Toward Continuum Robot Tentacles for Lung Interventions: Exploring Folding Support Disks," *IEEE Robot. Autom. Lett.*, vol. 8, no. 6, pp. 3494–3501, Jun. 2023.
- [3] Q. Chen, M. Li, H. Wu, W. Liu, and J. Peng, "Design, self-calibration and compliance control of modular cable-driven snake-like manipulators," *Mechanism and Machine Theory*, vol. 193, p. 105562, Mar. 2024.
- [4] T. Liu, T. Yang, W. Xu, G. Mylonas, and B. Liang, "Efficient Inverse Kinematics and Planning of a Hybrid Active and Passive Cable-Driven Segmented Manipulator," *IEEE Trans. Syst. Man Cybern. Syst.*, vol. 52, no. 7, pp. 4233–4246, Jul. 2022.
- [5] Z. Hu, H. Yuan, W. Xu, T. Yang, and B. Liang, "Equivalent kinematics and pose-configuration planning of segmented hyper-redundant space manipulators," *Acta Astronautica*, vol. 185, pp. 102–116, Aug. 2021.
- [6] S. Ma, B. Liang, and T. Wang, "Dynamic analysis of a hyper-redundant space manipulator with a complex rope network," *Aerospace Science and Technology*, vol. 100, p. 105768, May 2020.
- [7] M. Luo, Y. Tian, E. Li, M. Chen, and M. Tan, "A Local Obstacle Avoidance and Global Planning Method for the Follow-the-Leader Motion of Coiled Hyper-Redundant Manipulators," *IEEE Trans. Ind. Inf.*, vol. 20, no. 4, pp. 6591–6602, Apr. 2024.
- [8] A. Gao *et al.*, "Body Contact Estimation of Continuum Robots With Tension-Profile Sensing of Actuation Fibers," *IEEE Trans. Robot.*, vol. 40, pp. 1492–1508, 2024.
- [9] B. Lin, W. Xu, W. Li, H. Yuan, and B. Liang, "Ex Situ Sensing Method for the End-Effector's Six-Dimensional Force and Link's Contact Force of Cable-Driven Redundant Manipulators," *IEEE Trans. Ind. Inf.*, vol. 20, no. 5, pp. 7995–8006, May 2024.
- [10] N. G. Cheng *et al.*, "Design and Analysis of a Robust, Low-cost, Highly Articulated manipulator enabled by jamming of granular media," in *2012 IEEE International Conference on Robotics and Automation*, St Paul, MN, USA: IEEE, May 2012, pp. 4328–4333.
- [11] Y.-J. Kim, S. Cheng, S. Kim, and K. Iagnemma, "A Stiffness-Adjustable Hyperredundant Manipulator Using a Variable Neutral-Line Mechanism for Minimally Invasive Surgery," *IEEE Trans. Robot.*, vol. 30, no. 2, pp. 382–395, Apr. 2014.
- [12] C. Yang *et al.*, "Geometric constraint-based modeling and analysis of a novel continuum robot with Shape Memory Alloy initiated variable stiffness," *The International Journal of Robotics Research*, vol. 39, no. 14, pp. 1620–1634, Dec. 2020.
- [13] C. Li *et al.*, "A Miniature Manipulator With Variable Stiffness Towards Minimally Invasive Transluminal Endoscopic Surgery," *IEEE Robot. Autom. Lett.*, vol. 6, no. 3, pp. 5541–5548, Jul. 2021.
- [14] B. Zhao, L. Zeng, Z. Wu, and K. Xu, "A continuum manipulator for continuously variable stiffness and its stiffness control formulation," *Mechanism and Machine Theory*, vol. 149, p. 103746, Jul. 2020.
- [15] J. Lai, B. Lu, and H. K. Chu, "Variable-Stiffness Control of a Dual-Segment Soft Robot Using Depth Vision," *IEEE/ASME Trans. Mechatron.*, vol. 27, no. 2, pp. 1034–1045, Apr. 2022.
- [16] L. Zhang, Y. Gao, Z. Mu, L. Yan, Z. Li, and M. Gao, "A Variable-Stiffness Planning Method Considering Both the Overall Configuration and Cable Tension for Hyper-Redundant Manipulators," *IEEE/ASME Trans. Mechatron.*, vol. 29, no. 1, pp. 659–667, Feb. 2024.
- [17] X. Zheng, T. Yang, X. Zhu, Z. Chen, X. Wang, and B. Liang, "Dynamic modeling and experimental verification of a cable-driven continuum manipulator with cable-constrained synchronous rotating mechanisms," *Nonlinear Dyn.*, vol. 107, no. 1, pp. 153–172, Jan. 2022.
- [18] J. Li, W. Xu, W. Li, L. Yan, and B. Liang, "Design and Development of Composite Linkage Mechanism for Cable-Driven Segmented Manipulator to Increase Synchronous Accuracy and Transmission Distance," *IEEE Robot. Autom. Lett.*, vol. 9, no. 1, pp. 25–32, Jan. 2024.
- [19] R. Yasin and N. Simaan, "Joint-level force sensing for indirect hybrid force/position control of continuum robots with friction," *The International Journal of Robotics Research*, vol. 40, no. 4–5, pp. 764–781, Apr. 2021.

- [20] D. Sui, S. Zhao, T. Wang, Y. Liu, Y. Zhu, and J. Zhao, "Design of a Bio-inspired Extensible Continuum Manipulator with Variable Stiffness," *J Bionic Eng.*, vol. 22, no. 1, pp. 181–194, Jan. 2025.
- [21] H. Yuan, Z. Li, and W. Xu, "Kinetostatics for variable cross-section continuum manipulators," in *2021 IEEE International Conference on Robotics and Automation*, Xi'an, China: IEEE, May 2021, pp. 11878–11883.
- [22] E. Amanov, T.-D. Nguyen, and J. Burgner-Kahrs, "Tendon-driven continuum robots with extensible sections—A model-based evaluation of path-following motions," *The International Journal of Robotics Research*, vol. 40, no. 1, pp. 7–23, Jan. 2021.
- [23] X. Wang, Q. Lu, D. Lee, Z. Gan, and N. Rojas, "A Soft Continuum Robot With Self-Controllable Variable Curvature," *IEEE Robot. Autom. Lett.*, vol. 9, no. 3, pp. 2016–2023, Mar. 2024.
- [24] S. Lyu, P. Yao, H. Xiao, W. Zhang, and X. Ding, "Approximating cylinders with bundle-folding plane-symmetric Bricard linkages," *International Journal of Mechanical Sciences*, vol. 221, p. 107231, May 2022.
- [25] T.-W. Liu, J.-B. Bai, N. Fantuzzi, and X. Zhang, "Thin-walled deployable composite structures: A review," *Progress in Aerospace Sciences*, vol. 146, p. 100985, Apr. 2024.
- [26] D. E. Whitney, "The Mathematics of Coordinated Control of Prosthetic Arms and Manipulators," *Journal of Dynamic Systems, Measurement, and Control*, vol. 94, no. 4, pp. 303–309, Dec. 1972.
- [27] N. Simaan, "Snake-Like Units Using Flexible Backbones and Actuation Redundancy for Enhanced Miniaturization," in *Proceedings of the 2005 IEEE International Conference on Robotics and Automation*, Barcelona, Spain: IEEE, 2005, pp. 3012–3017.
- [28] R. E. Goldman, A. Bajo, and N. Simaan, "Compliant Motion Control for Multisegment Continuum Robots With Actuation Force Sensing," *IEEE Trans. Robot.*, vol. 30, no. 4, pp. 890–902, Aug. 2014.



Deshan Meng (Member, IEEE) received the Ph.D. degree in control science and engineering from the Department of Mechatronics and Automation, Shenzhen Graduate School, Harbin Institute of Technology, Shenzhen, China, in 2017.

He is currently an Associate Professor with the School of Aeronautics and Astronautics, Shenzhen Campus of Sun Yat-sen University, Shenzhen, China. His research interests include space robotics, cable-driven robots, and multibody system dynamics and control.



Taowen Guo received the B.E. degree in mechanical engineering from Chongqing Jiaotong University, Chongqing, China, in 2023. He is currently working toward the M.E. degree in mechanical engineering with the School of Aeronautics and Astronautics, Shenzhen Campus of Sun Yat-sen University, Shenzhen, China.

His research interests include mechanical design, modeling, and cable-driven robots.



Zhihao Ma received the B.E. degree in mechanical engineering from Tiangong University, Tianjin, China, in 2021, and the M.E. degree in mechanical engineering from Shenzhen Campus of Sun Yat-sen University, Shenzhen, China, in 2024. He is currently an engineer with the Qi Yuan National Laboratory.

His research interests include mechanical design, perception, planning, and control of unmanned systems.



Ruiqi Wang is currently a Ph.D. candidate in the Department of Automation at Tsinghua University. He obtained the B.E. degree from the School of Mechanical and Electrical Engineering at Harbin Institute of Technology in 2018 and the M.E. degree from the Department of Automation at Tsinghua University in 2022.

His research interests include modeling and control of robots.



Ziwei Wang (Member, IEEE) received the B.S. degree in automation from the Department of Control Science and Technology, Harbin Institute of Technology, Harbin, China, in 2016, and the Ph.D. degree in automation from the Department of Automation, Tsinghua University, Beijing, China, in 2020.

He is currently a Lecturer in Robotics at Lancaster University.



Xinliang Li received the B.E. and the M.E. degrees from Liaoning University of Science and Technology in 2011 and Huazhong University of Science and Technology in 2013.

Since 2014, he has successively worked in the Shenzhen International Graduate School of Tsinghua University, the Research Institute of Tsinghua University in Shenzhen, and Shenzhen Campus of Sun Yat-sen University, mainly engaged in the research work of space manipulator design, testing and environmental testing.



Xueqian Wang (Member, IEEE) received the Ph.D. degree in control science and engineering from the Harbin Institute of Technology, Harbin, China, in 2010.

He is currently a Professor and the Leader with the Center of Intelligent Control and Telescience, Tsinghua Shenzhen International Graduate School, Tsinghua University, Shenzhen, China. His research interests include dynamics modeling, control and teleoperation of robotic systems.



Bin Liang (Senior Member, IEEE) received the Ph.D. degree in mechanical automation from the Department of Precision Instrument, Tsinghua University, Beijing, China, in 1994.

Since 2007, he has been a Professor with the Department of Automation, Tsinghua University. His research interests include modeling and control of dynamic systems.